

Received April 10, 2019, accepted April 29, 2019, date of publication May 1, 2019, date of current version May 13, 2019.

Digital Object Identifier 10.1109/ACCESS.2019.2914377

Design of a Magnetic Induction Tomography System by Gradiometer Coils for Conductive Fluid Imaging

JINXI XIANG^{ID}¹, (Student Member, IEEE), YONGGUI DONG^{ID}¹, MAOMAO ZHANG², AND YI LI²

¹State Key Laboratory of Precision Measurement Technology and Instruments, Department of Precision Instrument, Tsinghua University, Beijing 100084, China

²Graduate School, Tsinghua University, Shenzhen 518055, China

Corresponding author: Yonggui Dong (dongyg@mail.tsinghua.edu.cn)

This work was supported in part by the National Natural Science Foundation of China under Grant 61671270.

ABSTRACT Magnetic induction tomography (MIT) is a non-intrusive and non-invasive method that can image the cross-sectional conductivity distribution inside the object without contact. Target applications are conductive fluid testing in biomedical or industrial processes. The gradiometer coil is used as the front-end sensor of the proposed MIT system. As demonstrated through theoretical analysis and numerical simulation, the phase sensitivity to the conductivity of the gradiometer is greatly enhanced by eliminating the primary voltage with differential coils. The sensitivity is tunable by the residual voltage. The experimental test illustrates that $2^{\circ}/(\text{Sm}^{-1})$ sensitivity can be achieved at 10 MHz. The eight-channel MIT system MIT hardware is based on a dual-channel data acquisition board PCI-5122 at 100-MS/S sample rate per channel and a waveform generator PCI-5412 as the 10-MHz excitation source. One frame of data contains 64 phase measurements, and each is calculated with the built-in fast Fourier transform (FFT) function on LabVIEW. With full-period sampling and averaging, the sensor array can achieve less than 5-m° phase noise. The system yields good long-term stability with a phase drift less than 20 m° over 4 h. We use a FEM model to solve the forward problem and then reconstruct the 2D images by a one-step Laplacian regularization algorithm. The experimental phantom tests show that the system is capable of imaging the conductivity distribution and also indicate that the images' quality becomes better by tuning an appropriate regularization coefficient.

INDEX TERMS Conductive fluid, gradiometer coil, inverse problem, Laplacian regularization, magnetic induction tomography.

I. INTRODUCTION

Cross-sectional imaging (or tomography) of the spatial electrical conductivity distribution inside a pipe or the human body has been an active research goal in instrumentation technology. Compared with the conventional single-point measurement, tomography can provide further information indicating the true state of the measured object. The applications to image conductive fluid (mostly lower than 10 S/m [1]) are of particular interest, because these are found in certain industrial processes [2], [3] and medical applications [4], [5]. Two typical low conductivity applications are imaging the saline water in multiphase flows [6] and imaging cerebral stroke [7]. For oil field production, non-intrusive and non-invasive

measurement of water volumetric flowrate in pipelines and separators is important for controlling productivity [8]. Other industrial applications includes oil-saline separation process of the crude oil production [9] and water contamination treatment [10]. For clinical diagnosis, imaging the position and the size of the hematoma are vital to diagnose the stroke which is a major cause of mortality.

Magnetic induction tomography (MIT), also known as electromagnetic tomography (EMT), is a relatively new process tomography modality aimed at imaging the distribution of permeability and/or conductivity. Its low cost, non-radiative, non-intrusive and non-invasive features make this technique extremely attractive. Compared with other hard-field tomography modalities, it has great potential in large-scale industrial processes, which cannot be achieved by such as magnetic resonance imaging and ultrafast X-ray [11].

The associate editor coordinating the review of this manuscript and approving it for publication was Lusheng Zhai.

Compared with its counterpart technique Electrical Impedance Tomography (EIT), MIT has the advantage that it does not require direct contact with the object. Therefore, MIT avoids the errors that are related to electrode contact impedances. MIT can look better through insulating layers, e.g. pipe which is made of rubber or skull which is made of bone tissue [12]. All the applications applicable to EIT are potential applications for MIT. Similar non-contact and non-intrusive characteristics are also exhibited by Electrical Capacitance Tomography(ECT) which operates effectively through an air gap for imaging of dielectric materials (electrical permittivity (ϵ)), but ECT is unsuitable for conductive materials ($\sigma \gg \omega\epsilon$) because the air layer dominates the response.

MIT applies a primary magnetic field \mathbf{B} with an excitation coil. The distribution of the magnetic field depends on the arrangement of the sensors and the distribution of the material in the sensing area. This is also known as the soft-field effect. A secondary magnetic field $\Delta\mathbf{B}$ is then generated by the eddy current induced in the object. By measuring the resultant total field $\mathbf{B} + \Delta\mathbf{B}$, the distribution of the electric properties can be reconstructed with proper algorithms. As suggested in [11] [1], MIT systems can be divided into two categories: high-conductivity imaging for metal-related applications and low-conductivity imaging for conductive fluid imaging (biological and multiphase flow). The target applications of this paper fall into the latter category. The development of MIT for conductive fluid is more difficult because the electrical conductivities are many orders of magnitude lower than those of metals. A general challenge is that the response signal has a large common-mode voltage V_0 induced by primary field \mathbf{B} and an extremely small ΔV induced by secondary field $\Delta\mathbf{B}$ [12], giving that $|\Delta V/V_0| \ll 1$ because the conductivity is usually smaller than 2 S/m for biomedical measurement [13] and 10 S/m for industrial applications [1]. For example, $|\Delta V/V_0|$ can be as low as 10^{-7} at β -dispersion [14]. Digital acquisition of these signals requires an impractical high resolution ADC [15]. Therefore, it is strongly recommended to eliminate the induced common-mode signal V_0 so as to improve the signal dynamic range and signal-to-noise ratio (SNR) [16].

Significant efforts have been made in MIT system design. For the single sensing coil scheme, the requirements of the hardware system are more demanding without removing the primary field. Enhancement of the hardware resolution and SNR has been attempted with some successes by using down-conversion, digital demodulation, and high-performance commercial acquisition board. S. Watson *et al.* designed a 16-channel system that is capable of imaging conductivity below 10 S/m [1]. The system has a fixed operating frequency of 10 MHz and the received signal is heterodyne down-converted to make measurements. W. Yin *et al.* proposed a highly integrated digital MIT system for metal object imaging based on field programmable gate array (FPGA) [17]. Wei and Solemani developed a two-phase flow imaging experimental platform using the 16-channel MIT system.

The experimental results indicate that a conductivity contrast as small as 1.58 S/m can be imaged [18].

The differential configuration is a preferable solution for capacitive and inductive sensors to deal with the high common-mode signal and to enhance the dynamic range. Z. Cui *et al.* studied a differential configuration consisting of concentrically arranged dual array electrodes to cancel the standing capacitance for ECT and an average improvement of 10.8 dB in SNR was achieved [19]. E.J. Mohamad *et al.* applied two differential excitation potentials in ECT to increase the voltage across the center of the pipe and consequently, the linear relationship between the capacitances and the permittivity was improved dramatically [20]. H. Payseren *et al.* designed a gradiometric receive coil to attenuate the unwanted signal arising from the excitation field and a 17 dB lower background level was obtained compared to the conventional Tx-Rx coil, which is crucial for detecting low amounts of magnetic nanoparticle [21]. The differential coil scheme has also been adopted in some reported MIT systems and there are some good examples. J. Rosell-Ferrer *et al.* presented a multi-frequency MIT with planar gradiometer to detect signal and to improve the ratio of $|\Delta V/V_0|$. The gradiometers were oriented in the z-direction producing an antisymmetric sensitivity map along the z-axis. [22]. Z. Xu *et al.* proposed a MIT in which the excitation coil and the detection coil are coaxially fixed, and an axial gradiometer was used as a detection coil to eliminate a primary magnetic field [16]. M. O'Toole *et al.* used receiver coils that are wound in a gradiometer arrangement for biomedical and metallic measurement in industrial scale applications. Lead-screw mechanism and tuning loops were used to balance the gradiometer precisely [23] [24]. Although previous works utilized gradiometer coil as an effective technique to cancel the primary field, more detailed and instructive analysis about the design parameters of the sensor is still not adequate.

This paper presents substantial sensor design about gradiometer coil (sensitivity, linearity, etc.) and develops an 8-channel MIT system using gradiometer coils as the front-end sensors. Both the measurement hardware and the image reconstruction algorithm are presented. There now follows descriptions of the gradiometer sensor in Section II, excitation and sensing electronics in Section III, forward and inverse problem in Section IV, system characteristics in Section V, and experimental results in Section VI.

II. GRADIOMETER COIL DESIGN

A. MEASUREMENT PRINCIPLE

In Fig. 1, two identical induction coils are placed coaxially at an equal distance from the excitation coil. An alternating current is applied to the excitation coil to generate a primary magnetic field. The eddy current is induced in the measurement target by the primary magnetic field. Therefore, a secondary magnetic field will be generated, which produces electromotive force in the sensing coil. Two sensing coils are

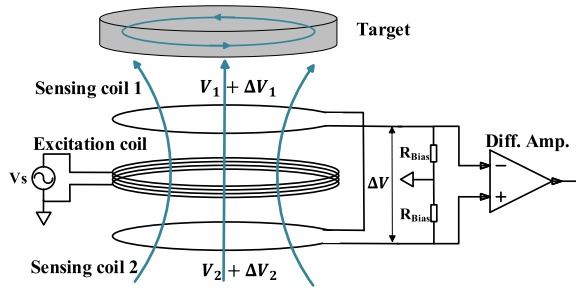


FIGURE 1. The principle of the gradiometer coil.

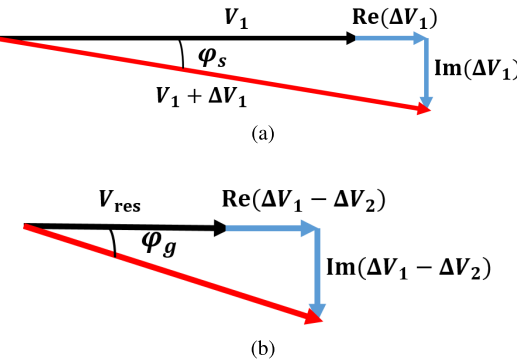


FIGURE 2. Phasor diagram representing the primary and secondary voltage. (a) Signal phasor diagram of sensing coil 1. (b) Signal phasor diagram of gradiometer coil.

connected in anti-phase to eliminate common mode signal and to pick up the differential signal.

The voltages induced by the secondary field in the sensing coils ΔV_1 and ΔV_2 can be expressed by a quasi-static approximation [1]:

$$\begin{cases} \frac{\Delta V_1}{V_1} = P_1 \omega \mu_0 [\omega \epsilon_0 (\epsilon_r - 1) - i\sigma] + Q_1 (\mu_r - 1), \\ \frac{\Delta V_2}{V_2} = P_2 \omega \mu_0 [\omega \epsilon_0 (\epsilon_r - 1) - i\sigma] + Q_2 (\mu_r - 1), \end{cases} \quad (1)$$

where V_1 and V_2 are the voltages induced by the primary field in sensing coil 1 and 2, respectively. σ , ϵ_r and μ_r are the electrical conductivity, relative permittivity and magnetic permeability of the target, ϵ_0 and μ_0 are the permittivity and permeability of free space, ω is the angular frequency of excitation signal, P_1 and Q_1 are the geometrical factors that depend on the size and shape of the target and its position relative to the coil. The same formula applies to sensing coil 2 but with different geometry factors P_2 , Q_2 . Fig. 2 represents the primary and secondary signals by the phasor diagram.

The real part of $\Delta V_1/V_1$ and $\Delta V_2/V_2$ is related to the change in relative permeability μ_r and permittivity ϵ_r while the imaginary part reflects the change in conductivity σ . The first term on the right side of equation (1) arises from the induced eddy current in the target, and the second term is from the magnetic polarization of the target. In this paper, only non-magnetic materials are considered ($\mu_r = 1$), so the second term on the right-hand side is zero.

The phase of the induced voltage in sensing coil 1 is derived from equation (1), since $\left| \frac{\Delta V_1}{V_1} \right| \ll 1$,

$$\varphi_s = \arctan \left\{ \frac{\text{Im}(\Delta V_1)}{V_1 + \text{Re}(\Delta V_1)} \right\} \approx \frac{\text{Im}(\Delta V_1)}{V_1} = -P_1 \omega \mu_0 \sigma \quad (2)$$

The sensitivity of the phase to conductivity:

$$s_s = \frac{\Delta \varphi_s}{\Delta \sigma} = -P_1 \omega \mu_0 \quad (3)$$

As for perfectly symmetric gradiometer coil, the distances from the two sensing coils to the excitation coil are equal and the central axis of the coil planes are aligned. In this situation, the primary voltages produced by the excitation coil in the sensing coils are equal ($V_1 = V_2 = V_0$) but connected in anti-phase. The secondary voltage in the two sensing coils ΔV_1 and ΔV_2 are not equal because of the different separation from the target ($P_1 \neq P_2$). Thus, the differential output of the gradiometer coil (in Fig. 1) is:

$$\begin{aligned} \Delta V &= \Delta V_1 - \Delta V_2 \\ &= (P_1 - P_2) \omega \mu_0 [\omega \epsilon_0 (\epsilon_r - 1) - i\sigma] V_0 \end{aligned} \quad (4)$$

The signal phase of the gradiometer coil is defined by:

$$\varphi_g = \arctan \left\{ -\frac{\sigma}{\omega \epsilon_0 (\epsilon_r - 1)} \right\} \quad (5)$$

The sensitivity of phase to conductivity is defined to be:

$$s_g = \frac{\Delta \varphi_g}{\Delta \sigma} = -\frac{a}{a^2 + \sigma^2} \quad (6)$$

where $a = \omega \epsilon_0 (\epsilon_r - 1)$. The sensitivity s_g of the gradiometer coil is non-linear in this case.

In practice, it is difficult to adjust the gradiometer coil to be symmetric perfectly. And more importantly, considering the nonlinearity of s_g in equation (6), it is unnecessary to do so. We are going to demonstrate that presenting a small residual voltage deliberately can preserve the linearity of the sensor. Modified from equation (4), the output of the gradiometer with a small residual voltage is:

$$\begin{aligned} \Delta V &= \Delta V_1 - \Delta V_2 + V_{\text{res}} \\ &= (P_1 - P_2) \omega \mu_0 [\omega \epsilon_0 (\epsilon_r - 1) - i\sigma] V_0 + V_{\text{res}} \end{aligned} \quad (7)$$

where $V_{\text{res}} = V_1 - V_2$ is the residual voltage due to the non-ideal symmetry of the gradiometer coil.

And the corresponding phase of gradiometer coil:

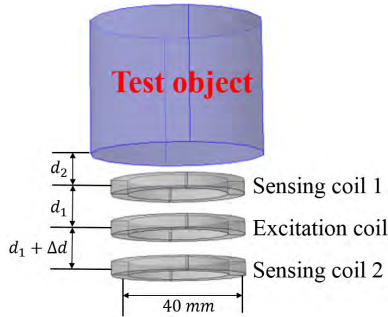
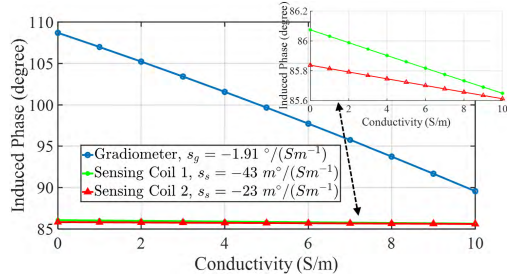
$$\varphi_g = \arctan \left\{ -\frac{V_0 (P_1 - P_2) \omega \mu_0 \sigma}{V_{\text{res}} + V_0 (P_1 - P_2) \omega \mu_0 \omega \epsilon_0 (\epsilon_r - 1)} \right\} \quad (8)$$

Assuming that $|V_{\text{res}}| \gg |(\Delta V_1 - \Delta V_2)|$, formula (8) simplifies to the form:

$$s_g \approx -\frac{V_0 (P_1 - P_2) \omega \mu_0}{V_{\text{res}}} \sigma \quad (9)$$

The resulting sensitivity ($V_{\text{res}} > 0$) of the gradiometer is:

$$s_g = \frac{\Delta \varphi_g}{\Delta \sigma} = -\frac{V_0 (P_1 - P_2) \omega \mu_0}{V_{\text{res}}} \quad (10)$$

**FIGURE 3.** Simulation model configuration.**FIGURE 4.** Sensitivity of the gradiometer and single-sensing coil sensor.

With the unknown geometrical factor P_1 and P_2 , the sensitivity enhancement of the gradiometer coil cannot be distinguished intuitively by comparing formula (3) and (10). Numerical simulations on COMSOL Multiphysics are employed in the following section to reveal the sensitivity enhancement of the gradiometer coil.

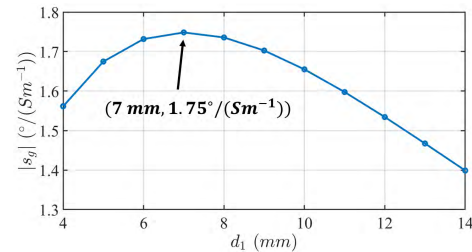
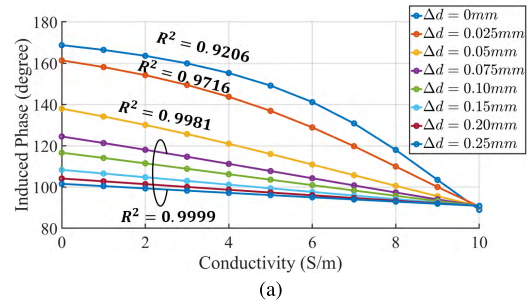
B. COMSOL SIMULATIONS

The theoretical analysis of gradiometer coil in Section II-A is validated on the AC/DC module of Comsol Multiphysics. A diagram of the gradiometer coil model together with a cylinder conductive test object is shown in Fig. 3. The excitation coil has 4 turns and the sensing coil has 8 turns. The distance from the sensor to the object d_2 is assumed to be fixed at 5 mm. A 10-MHz primary magnetic field is produced by applying 100 mA current at the excitation coil.

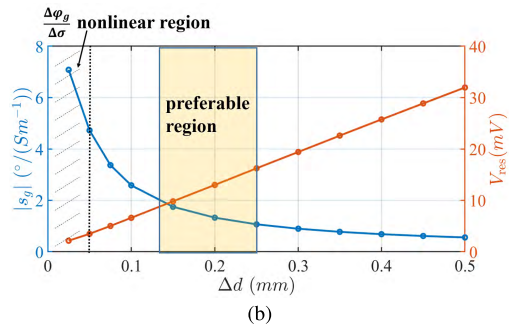
The output signal of the gradiometer coil is obtained by subtracting the induced signals in sensing coil 1 and 2. In this case, $d_1 = 6 \text{ mm}$, $\Delta d = 0.15 \text{ mm}$. The conductivity of the test object is changed from 0 S/m to 10 S/m. Fig. 4 shows the phase sensitivity to conductivity. The results show that the sensitivity of sensing coil 1 is $-0.043^\circ/(\text{Sm}^{-1})$, greater than that of sensing coil 2 $-0.023^\circ/(\text{Sm}^{-1})$ because sensing coil 1 is closer to the test object. In contrast, the sensitivity of the gradiometer s_g is $-1.91^\circ/(\text{Sm}^{-1})$. Significant sensitivity enhancement is demonstrated with a gradiometer coil compared to a single-sensing coil.

Two key design parameters of the gradiometer sensor are further discussed, namely d_1 (the distance between excitation coil and sensing coil) and Δd (the distance asymmetry, see Fig. 3).

In formula (10), as d_1 increases, the primary voltage V_0 would decrease since the magnetic flux across the sensing

**FIGURE 5.** Sensitivity s_g for different d_1 ($d_2 = 5 \text{ mm}$, $V_{\text{res}} = 11.7 \text{ mV}$).

(a)



(b)

FIGURE 6. Sensitivity s_g for different Δd ($d_1 = 6 \text{ mm}$, $d_2 = 5 \text{ mm}$).
(a) Plots of induced phase against the conductivity for different Δd .
(b) Sensitivity s_g and residual voltage V_{res} depends on Δd .

coils reduces but the geometrical difference ($P_1 - P_2$) would increase. In theory, there is an optimum value of the sensitivity s_g at some point. It is complicated to solve it analytically but it can be demonstrated by numerical simulation. By fixing the residual voltage V_{res} while changing d_1 , the corresponding s_g is obtained as shown in Fig. 5. An optimal s_g is achieved at $d_1 = 7 \text{ mm}$. It would be noteworthy that s_g is less sensitive to d_1 compared to Δd in Fig. 6.

Another important parameter is Δd . When $\Delta d = 0 \text{ mm}$, $V_{\text{res}} = 0$ since the gradiometer coil is perfectly symmetrical. As shown in Fig. 6 (a), the sensitivity is monotonic but nonlinear. The sensor is highly sensitive to changes in electrical conductivity at this state. When $\Delta d > 0$ ($V_{\text{res}} > 0$), larger Δd leads to increased V_{res} , which results in lower sensitivity but higher linearity. In Fig 6 (a), each line is a phase response for different Δd . The R^2 in the figure indicates how close the data are to the linear regression. As Δd increases, the R^2 of linear fitting enlarges correspondingly.

Fig 6 (b) shows that high sensitivity of the gradiometer can be achieved by a small Δd , but this would result in non-linearity of phase sensitivity and a smaller V_{res} meanwhile.

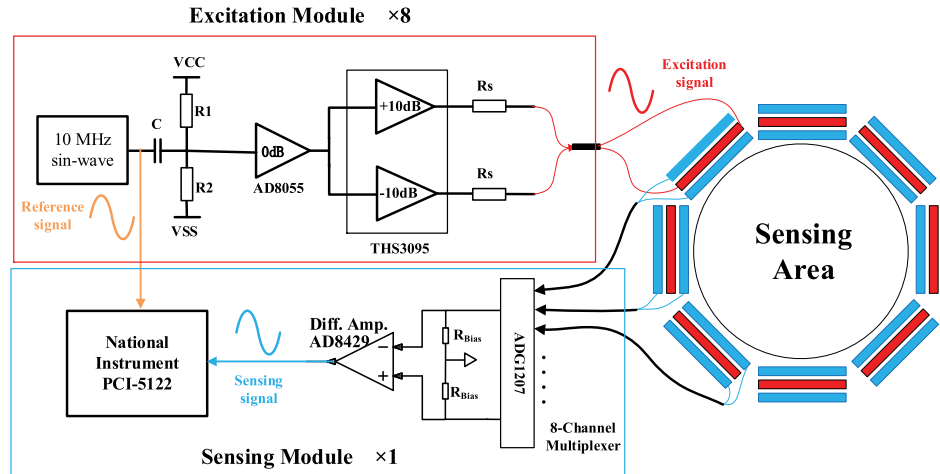


FIGURE 7. The 8-channel MIT system using gradiometer coils.

V_{res} should not be excessively small to ensure it does not fall below the noise level of the detectors. Therefore, due to the required SNR, the sensitivity s_g is confined by an upper bound. Another problem with an excessively small Δd is that it is mechanically unstable and vulnerable to vibration or displacement, causing a sensitivity drifting in practical usage. Fig 6 (b) illustrates the preferable region for compromising between the sensitivity and the stability & SNR.

In summary, the characteristics of the gradiometer coil, including sensitivity, linearity, and signal-to-noise ratio (SNR), depend on Δd and d_1 . An advised guideline for designing a gradiometer coil includes three steps:

- Set down the radius and the number of turns of the coil. The radius of the coil depends on the size of the sensing area and the optimum number of turns is a compromise between maximizing sensitivity and avoiding self resonance.
- Choose an appropriately large d_1 . The size of the sensor is prior to the sensitivity s_g when tuning d_1 because s_g is less sensitive to d_1 .
- Adjust Δd to get the required sensitivity and linearity. It is practical to observe V_{res} by an oscilloscope as an indicator of Δd instead of measuring Δd directly.

III. SYSTEM DESIGN

A. SYSTEM OVERVIEW

The MIT system (see Fig. 7) comprises four subsystems: (1) the sensor array consisting of 8 gradiometer coils; (2) the excitation circuits to drive gradiometer coils; (3) the signal conditioning circuit; (4) the measurement and channel switching module, including a FPGA board and a host computer.

The operation principle is as follows. One of the 8 excitation channels is selected and enabled. The 10-MHz signal source is provided by the National Instrument DAC board PCI-5412. The rest of the other 7 excitation channels are disabled as an open circuit. The 8 differential sensing coils are then sequentially enabled. The sensing signals are

multiplexed to the measurement module to measure the signal phase by using the excitation signal as a reference.

One frame of data consists of 64 phase values covering all the excitation/sensing coil combinations (8×8). For conductivity imaging, two frames of data are required, one frame with the test object within the sensing area and another reference frame for an empty detector space or some other conditions. An image of the conductivity distribution is then reconstructed with the proposed Laplacian regularization method (Section IV-B). The following sections describe details of the subsystems.

B. SENSOR ARRAY

Printed circuit board (PCB) is used to fabricate the proposed coils in a low-cost and simple manner because PCB coils are mechanically stable, consistent in fabrication, and easy to adjust the separation [25]. To minimize phase shift due to capacitive coupling, all coils are connected with twisted-pair cables that are electrostatically shielded outside.

We use planar coils without ferrite (Fig. 8 (a)). The sensing coil has 8 turns with a trace width of 10 mils and a spacing width of 10 mils between adjacent traces. The excitation coil has 4 turns with a larger trace width of 20 mils to carry stronger excitation current. The spacing width is 12 mils between adjacent traces. The average of the inner diameter and the outer diameter is 40 mm. The inductance of the sensing coil is $\sim 6.7 \mu\text{H}$ (10 MHz) and the inductance of the excitation coil is $\sim 1.7 \mu\text{H}$ (10 MHz). Measured with an impedance analyzer (Keysight E4990A), the resonance frequencies are 32.2 MHz and 41.0 MHz for sensing coil and excitation coil, respectively. To make a gradiometer sensor, two sensing coils and one excitation coils placed at 6 mm apart with plastic screws and nuts. Plastic gaskets are used to adjust the spacing between coils slightly.

The sensor array evenly arranges 8 gradiometers outside the circumference of 12 cm in diameter, as shown in Fig. 8 (b). There are 64 excitation/sensing combinations. Section II-A analyzes characteristics of the gradiometer coil sensor using

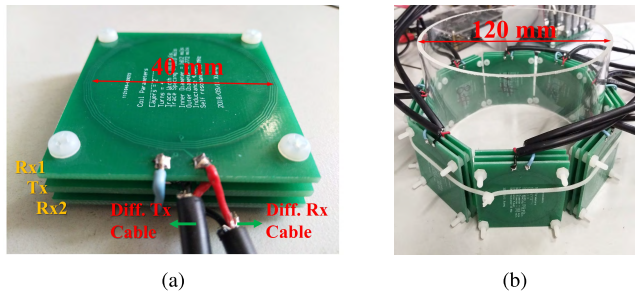


FIGURE 8. The 8-channel gradiometer sensor array. (a) One gradiometer coil. (b) Sensor array.

the combination where the axial angle between the excitation and the sensing coil is 0° as an example. The same physics applies to other combinations, but with different primary voltage and geometrical factor in formula (1). The spatial distribution of sensor sensitivity is revealed in Fig. 11.

C. EXCITATION CIRCUITS

The excitation signal source is generated by PCI-5412, a 14-bit 100 MS/s DAC from National Instrument. The output of the signal source is passed to a power amplifier with a differential current of approximately 80 mA r.m.s. The power amplifier THS3095 from Texas Instrument has a wide bandwidth of 210 MHz and a maximum current drive of 250 mA. It has a disable function pin that places the output into the high-impedance state. Through the disable function of the chip, 8 excitation coils are enabled sequentially. The differential current source connects with the coils through shielded twisted-pair cable to guarantee minimum magnetic interference. To ensure temperature stability, a metallic heat radiator is attached on the top of each power amplifier to dissipate the heat and a cooling fan is also used.

Two $5\ \Omega$ serial resistors R_s are added at the differential output of the power amplifier to avoid high current sink. As the coils are inductors, their load impedance increases proportionally with frequency. A high supply voltage is needed to drive a strong current at high frequency. To cope with this problem, we add a capacitor in series with the resistor to resonate the coils at 10 MHz, the desired frequency of the system [26]. This method works for a single operating frequency; to generate other frequencies requires different capacitors.

D. SIGNAL CONDITIONING CIRCUIT

The wideband analog multiplexer ADG1207 switches one of eight differential inputs to a common differential output to select the sensing signals. The input stage of the signal conditioning circuit is an instrument amplifier AD8429 that differentially amplifies the sensing signals. The differential input stage provides further rejection of unwanted interference due to capacitive coupling with the excitation coils. Two grounded resistors R_{Bias} are connected at the non-inverting and inverting input pins to provide an appropriate bias current for AD8429. They also create a closed loop for the

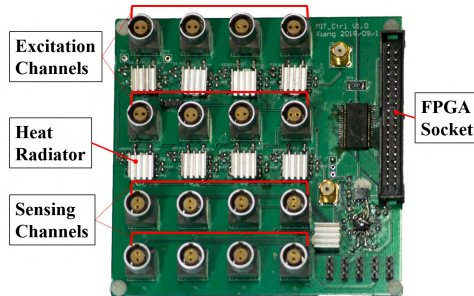


FIGURE 9. MIT circuit board.

induced current in sensing coils. Later, amplification with OPA690 enlarges the differential signal by 35 dB. A second-order Butterworth low pass filter with a cut-off frequency of 12 MHz is further used as an anti-aliasing filter to remove noise. The output signal is then passed to the dual-channel 14-bit data acquisition board PCI-5122.

After the sampling, the dual channel data are processed in LabVIEW. The phase of signals is measured with the Fast Fourier Transform (FFT) that is accomplished by a built-in FFT tone measurement module. Although other phase measurement methods are reported, FFT is fast and capable of achieving high precision up to sub-millidegree with full-period sampling and multiple averaging [27].

E. MEASUREMENT AND CHANNEL SWITCHING MODULE

This module includes an FPGA board and a host computer (see Fig. 19). The computer controls the DAC board PCI-5412 to generate a sinusoidal signal to power amplifiers and communicates with an FPGA board through a USB cable to control the operation of the excitation coils as well as the sequential measurement of the sensing coils. At the same time, dual-channel acquisition with PCI-5122 is controlled by the computer as well. The real-time measurement results are displayed and stored on the computer software programmed by LabVIEW.

IV. SENSITIVITY MAPS AND IMAGE RECONSTRUCTION

A. SENSITIVITY MAPS

The linear model describing phase change $\Delta\Phi$ and the conductivity change $\Delta\sigma$ is generally expressed as:

$$\Delta\Phi = S\Delta\sigma \quad (11)$$

Sensitivity matrix S is the prior information of image reconstruction that maps the conductivity distribution to phase values. It consists of self-inductance and mutual inductance values covering all excitation and sensing coil combinations. The combination of each element sensitivity can be used to describe the sensing field due to the fact that it is discretized into N elements ($N = 3260$ in this paper).

The sensitivity matrix S is solved based on the reciprocity theorem [28]:

$$S = \frac{\Delta Z}{\Delta\sigma} \approx \frac{-v}{I_1 I_2} \mathbf{E}_1 \cdot \mathbf{E}_2 \quad (12)$$

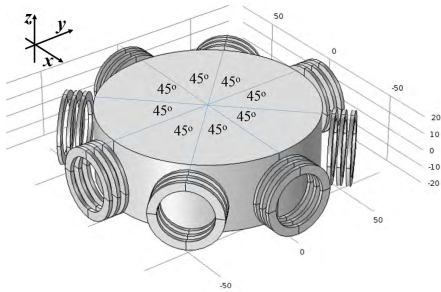


FIGURE 10. The COMSOL model for MIT sensitivity maps calculation.

where ΔZ is the transfer-impedance change. $\Delta\sigma$ is the conductivity change in the sensing area. v is the voxel of the discretization mesh in COMSOL. \mathbf{E}_1 is the electric field produced by a current I_1 injecting into the excitation coil. \mathbf{E}_2 is the electric field produced by a current I_2 injecting into the differential sensing coil.

Sensitivity matrix in (12) has been previously reported and widely used. It reveals that the sensitivity coefficient for conductivity at any point in the object should be the dot product of the two electric fields [29]. The dot product of \mathbf{E}_1 and \mathbf{E}_2 in (12) is further expressed as [28]:

$$\mathbf{S} = k \mathbf{B}_1 \mathbf{B}_2 \quad (13)$$

where \mathbf{B}_1 is the magnetic field produced by a current I_1 injecting into the excitation coil, \mathbf{B}_2 is the magnetic field produced by a current I_2 injecting into the differential sensing coil, k is a coefficient.

The 2D MIT sensitivity maps matrix is calculated using COMSOL Multiphysics and Matlab with a 1:1 sensor model as shown in Fig. 10. In a homogeneous space, the 8-channel MIT system has 64 sensitivity maps considering all excitation and sensing combinations, whereas among them only five maps are unique because of the symmetric structure. The axial angles between the excitation coil and the sensing coils of the five unique maps are $0^\circ, 45^\circ, 90^\circ, 135^\circ, 180^\circ$. The COMSOL simulation model is 3-D and the sensitive maps should be 3-D theoretically. To simplify the reconstruction problem, only the average value of conductivity in the z-axis direction is considered. The two-dimensional sensitive maps in the X-Y plane are obtained by summing up the sensitivity values in the z-axis direction.

Fig. 11 demonstrates the five unique sensitivity maps. There are three distinct features of these sensitivity maps:

- (1) There is a tubular sensitive area connecting the excitation coil and the sensing coil. Away from this area, the sensitivity is basically small. This could be explained that the inductive sensors are sensitive only to the flux that is perpendicular to their main axis [30].
- (2) The sensitivity is high at the close proximity to the coils. This characteristic is similar to the sensitivity maps of other soft-field modalities like ECT and EIT.
- (3) At the center of MIT sensor array, the sensitivity is low because the magnetic field generated by the inductive coil is divergent [31].

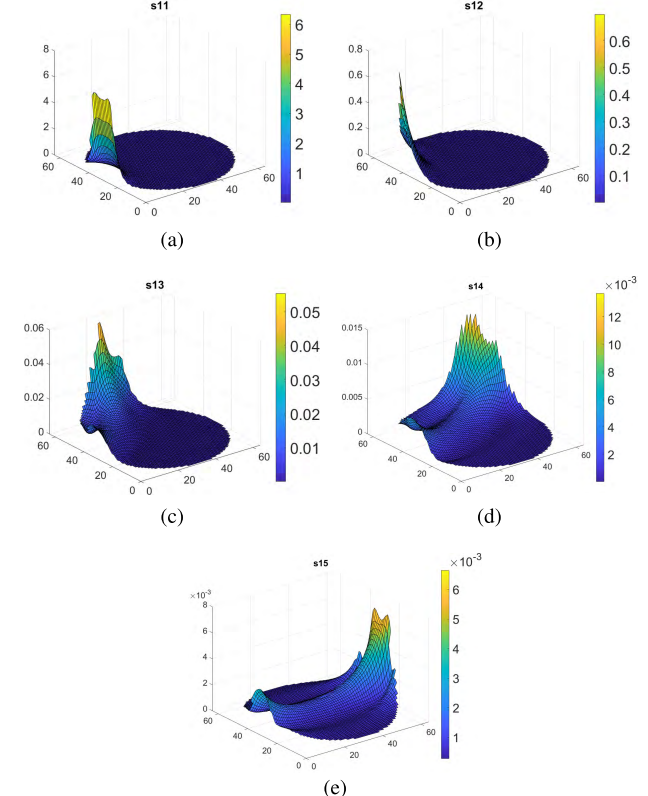


FIGURE 11. MIT sensitivity maps. (a) s_{11} (0°). (b) s_{12} (45°). (c) s_{13} (90°). (d) s_{14} (135°). (e) s_{15} (180°).

B. IMAGE RECONSTRUCTION

The purpose of the MIT image reconstruction is to estimate the conductivity distribution inside the object, given a set of phase measurement around the object. Image reconstruction is accomplished by solving an ill-posed and nonlinear inverse problem. Based on the measured phase of the induced voltage $\Delta\Phi$, the optimal estimation $\hat{\Delta\sigma}$ of the unknown conductivity distribution $\Delta\sigma$ is retrieved. It is described as the following optimization problem:

$$T_\alpha(\mathbf{m}) = \arg \min_{\hat{\Delta\sigma} \in \mathbb{R}^N} \left\{ \|\mathbf{S}\hat{\Delta\sigma} - \Delta\Phi\|_2^2 + \alpha \|L\mathbf{z}\|_p^p \right\} \quad (14)$$

where α is the regularization coefficient and L is the regularization matrix. $1 \leq p \leq \infty$ is related to the so-called L_p norm. When $p = 2$, it is the Tikhonov regularization method, and the resulting image edges are smooth and blurred. When $p = 1$, the method is Total Variation with a penalty of $L1$ that preserves the edge of the image. One iterative way to optimize (14) is by writing it into the quadratic programming form that can be solved by the interior point algorithm [32].

As for the non-iterative method, the one-step solution of the regularization method is expressed as (15).

$$\hat{\Delta\sigma} = (\mathbf{S}^T \mathbf{S} + \alpha \mathbf{L}^T \mathbf{L})^{-1} \mathbf{S}^T \Delta\Phi \quad (15)$$

where \mathbf{L} represents the second-order Laplacian operator matrix [33], being added to make the image smoother. The computation cost of this method is relatively low which facilitates its real-time implementation.

-1.3	-6.0	-1.3
-6.0	29.2	-6.0
-1.3	-6.0	-1.3

(a)

-6.1	-8.8	-6.1
-8.8	59.6	-8.8
-6.1	-8.8	-6.1

(b)

FIGURE 12. 2D Laplacian operator applied to a voxel. (a) $\theta = 1$. (b) $\theta = 2$.

The key parameter of the Laplacian matrix \mathbf{L} is the edge weight. Instead of fixing the weights like [33], we define the weight of an edge connecting vertices i and j via a thresholded Gaussian kernel weighting function [34].

$$W_{i,j} = \begin{cases} c \cdot \exp\left(-\frac{[\text{dist}(i,j)]^2}{2\theta^2}\right) & \text{if } \text{dist}(i,j) \leq L_w \\ 0 & \text{otherwise} \end{cases} \quad (16)$$

where $\text{dist}(i,j)$ is Manhattan distance between vertice i and the vertice j , and θ is a pre-defined parameter. The window length L_w of the Laplacian matrix \mathbf{L} is adjusted according to the required image smoothness. Fig. 12 shows two Laplacian matrices for different θ when $L_w = 3$, $c = 10$.

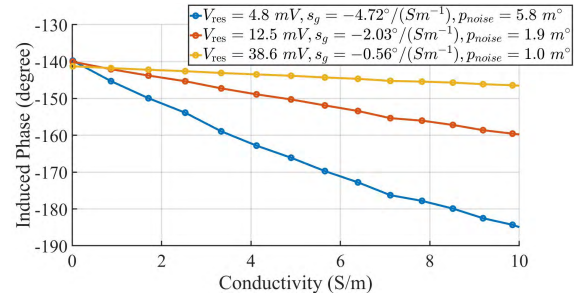
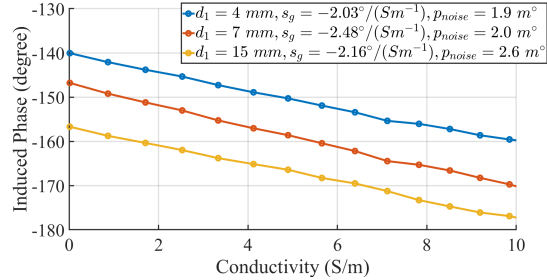
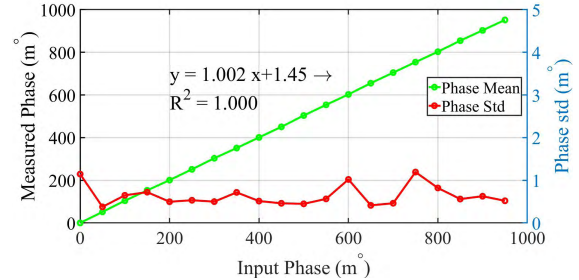
V. SYSTEM CHARACTERISTICS

A. SENSOR SENSITIVITY

The sensitivity experiment was carried out on a single-channel gradiometer. Sodium chloride solution with $0.01 \text{ S/m} \sim 10 \text{ S/m}$ was used to test the measurement performance of gradiometer for low conductivity objects. The NaCl solution in plastic bottles with 50 ml was placed close to the sensing coil. The bottom of the plastic bottom is 2 mm. The excitation coil is driven with 50 mA r.m.s., 10-MHz sinusous signal. When the experiment was conducted, the ambient temperature is 25°C .

In Fig. 13, the phase sensitivity of the gradiometer sensor are $-4.72^\circ/(Sm^{-1})$, $-2.03^\circ/(Sm^{-1})$, and $-0.56^\circ/(Sm^{-1})$ for three different V_{res} . The phase change is negative and proportional to conductivity, in close agreement with the theoretical equation (10). The phase noise of the three curves are 5.8 m° , 1.9 m° , and 1.0 m° . The results indicate that gradiometer with higher sensitivity has a larger measurement noise because V_{res} is smaller, making it more susceptible to noise and external interference. Therefore, there is a trade-off between the sensitivity and the noise level.

Fig. 14 shows that the sensitivity is less sensitive to d_1 as analyzed in Section II-B. The phase noises of three d_1 are at the same level approximately. The phase offset of three curves in Fig. 14 may due to changes in capacitive coupling between coils, which is caused by the change of separation between coils. The phase offset will not make a difference because only phase change is used for image reconstruction.

**FIGURE 13.** Sensitivity s_g for different V_{res} (experimental data, $d_1 = 4 \text{ mm}$, $d_2 = 5 \text{ mm}$).**FIGURE 14.** Sensitivity s_g for different d_1 (experimental data, $V_{\text{res}} \approx 12.5 \text{ mV}$, $d_2 = 5 \text{ mm}$).**FIGURE 15.** Phase measurement linearity.

B. PHASE LINEARITY

To evaluate the phase linearity, the phase difference of the driving signal and the reference signal was generated from 0 to 1000 millidegree with a step of 50 millidegree with a signal generator AFG3022B (Tektronix). The operation frequency was set to 10 MHz. The sampling rate of the PCI-5122 is 100 MSPS. The phase was measured by FFT tone module in LABVIEW. 30 phase values were averaged to reduce the measurement uncertainty. The phase linearity and the phase noise at each point are shown in Fig. 15.

A linear regression model was applied to the results in order to evaluate the linear relationship between the ground truth phase and the measured phase. The correlation coefficient (R^2) value of the linear regression model is 1.0000 and the phase noise (standard deviation) is mostly within 1 m° .

C. PHASE NOISE

The phase noise was measured by calculating the standard deviation of the phase measurement over 30 phase samples. To determine the noise of the system, a frame of data was collected with no test object present in the array. The phase

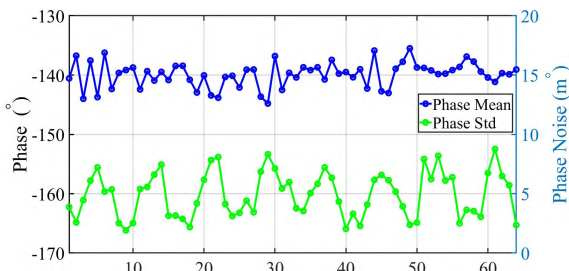


FIGURE 16. Phase mean and noise of the MIT system.

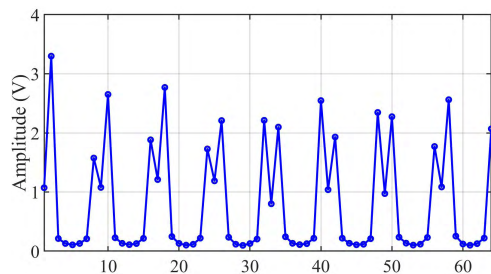


FIGURE 17. Signal amplitude of one frame of data.

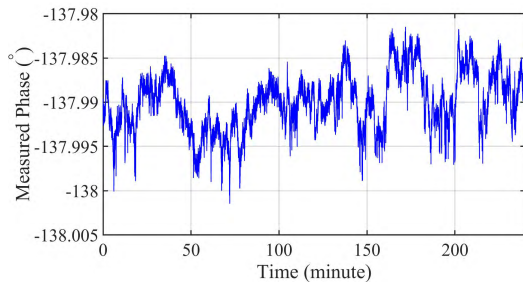


FIGURE 18. Phase drift (20 m° in 4 hours).

was computed for all 64 excitation/sensing combinations. The mean and the standard deviation (noise) of 30 phase value for each combination channel was calculated. The system's average noise was calculated by averaging over all 64 channel combinations.

The result in Fig. 16 shows that the maximum phase noise does not exceed 10 m° and the average phase noise of the 64 phase measurement is 4.9 m° . The phase noise show a periodic variation that is closely related with the amplitude of the induced voltage (as shown in Fig. 17). Since the noise level of the MIT hardware system is relatively constant throughout the measurement, a larger signal amplitude associates with a larger SNR of the received signals, resulting in smaller phase noise as shown in Fig. 16.

D. PHASE DRIFT

Phase drift represents the long-term stability of the system. In order to determine the drift of the system, 240 phase measurements are collected at a 1-minute interval. The total measurement time is 4 hours. The drift is calculated by measuring the difference between the maximum and minimum values of all measurements for each excitation/sensing combination.

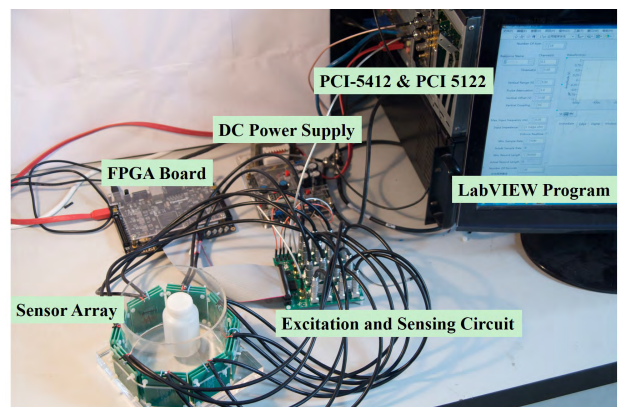


FIGURE 19. The experimental setup of the 8-channel MIT system for phantom test.

Then the phase drift of the system is defined as the average of all channel combinations.

Phase drift is shown in Fig. 18. The maximum phase drift within four hours was 20 m° . The results suggest that with properly designed of the system mechanisms, such as hardware chassis, metal radiator, and cooling fan, the observed phase drift is low. These mechanisms are considered to be capable of protecting the hardware from external interference, such as temperature change.

VI. IMAGE RECONSTRUCTION EXPERIMENTS

A. EXPERIMENT SETUP

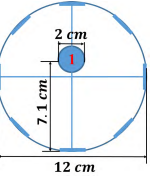
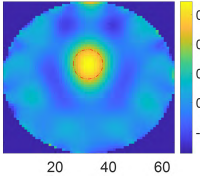
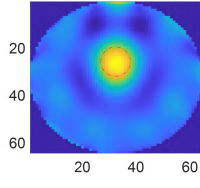
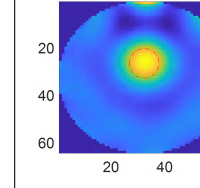
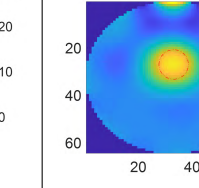
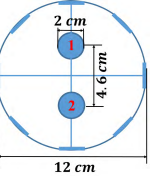
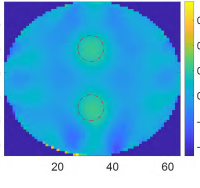
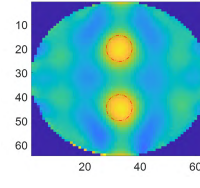
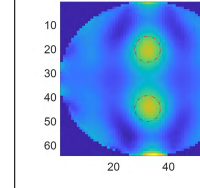
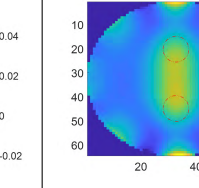
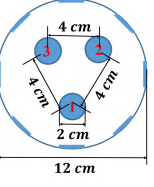
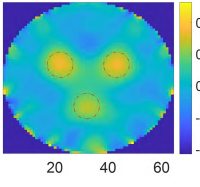
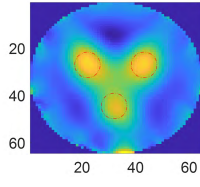
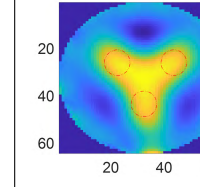
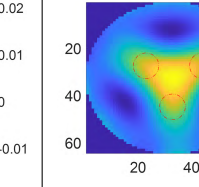
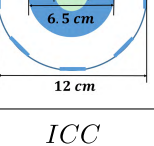
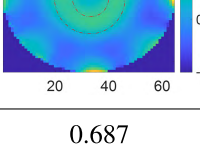
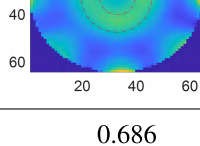
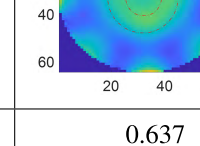
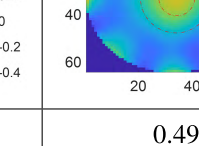
Several experimental tests were carried out to show the capability of the MIT system for conductive fluid applications. Four phantoms are applied, that is, one-object, two-object, three-object, and annular phantom that simulates annular flow. The first three phantoms are simulated by placing 2-cm diameter plastic bottles filling with NaCl solution in the sensing area of the MIT system. The annular phantom is simulated with a 6.5-cm diameter bottle holding the NaCl solution and a 2.8-cm diameter bottle that drains off the solution. The conductivity of all sodium chloride solutions in this experiment is 2 S/m .

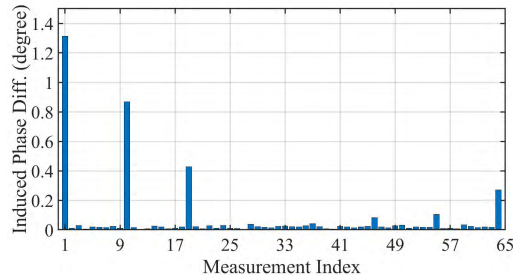
The excitation coils are driven by 10-MHz, 80 mA r.m.s. current. And 8 differential sensing coils are sequentially enabled and acquired with 100 MSPS sample rate to the measures the phase shift. It takes 20 seconds to get a frame containing 64 phase values. The frame rate is primarily constrained by the serial data acquisition sequence and long downloading time of PCI-5122. Frame rate could be accelerated with more parallel data acquisition channels.

In Fig. 19, the system configuration shows the experimental setup of MIT system. The system consists of a sensor array with 8 coils of gradiometer, an FPGA board, an excitation and sensing circuit, a data acquisition system based on National Instrument (NI) and a host computer.

It is a good practice to warm up the system for 15 minutes before measurement. Because when the circuit is powered on, the temperature of the components gradually increases. It takes time to reach a balanced state of the circuits.

TABLE 1. Phantom experiment with laplacian regularization.

Phantom	$\alpha = 1 \times 10^{-6}$	$\alpha = 1 \times 10^{-5}$	$\alpha = 1 \times 10^{-4}$	$\alpha = 1 \times 10^{-3}$
				
<i>ICC</i>	0.677	0.708	0.707	0.624
				
<i>ICC</i>	0.518	0.604	0.564	0.354
				
<i>ICC</i>	0.534	0.570	0.509	0.435
				
<i>ICC</i>	0.687	0.686	0.637	0.493

**FIGURE 20.** 64 phase change values of Phantom 1.

In general, the measurement values are unstable before warming up. Fig. 20 illustrates one frame of phase change obtained from Phantom 1. The background frame for reference is homogeneously filled with air.

B. EXPERIMENT RESULTS

The image correlation coefficient (*ICC*) is used to quantitatively evaluate the image quality between the reconstructed and the ground truth conductivity [33]. A larger value of

correlation coefficient suggests a better image quality. *ICC* is defined by:

$$ICC = \frac{\sum_{i=1}^N (\Delta\hat{\sigma}_i - \Delta\hat{\sigma}_{avr})(\Delta\sigma_i - \Delta\sigma_{avr})}{\sqrt{\sum_{i=1}^N (\Delta\hat{\sigma}_i - \Delta\hat{\sigma}_{avr})^2 \sum_{i=1}^N (\Delta\sigma_i - \Delta\sigma_{avr})^2}} \quad (17)$$

where N is the number of pixels and in this work $N = 3260$; $\Delta\hat{\sigma}_i$ and $\Delta\hat{\sigma}_{avr}$ are the i^{th} element and the average of the reconstructed conductivity variation; $\Delta\sigma_i$ and $\Delta\sigma_{avr}$ are the i^{th} element and the average of the true conductivity variation, respectively.

Table 1 summarizes the experimental results for four phantom tests by tuning the coefficient α of one-step Laplacian regularization in formula (15) from 10^{-6} to 10^{-3} . And *ICC* is calculated for each reconstructed image in the table.

Phantom 1 was designed to evaluate the reconstruction performance of single object. The reconstructed image is prominent and stable with the tuning parameter α . From 1×10^{-6} to 10^{-3} , the position of the target is clear and the

shape is distinct. The image artifact is the smallest at 1×10^{-5} where the largest *ICC* is obtained. Phantom 2 and 3 evaluated the reconstruction performance of multiple objects with close locations. The reconstructed results of Phantom 2 show that the two objects are clustered into a big pixel group due to the low spatial resolution if the regularization coefficient α exceeds 1×10^{-3} . But, conversely, a smaller α results in weaker regularization effect. $\alpha = 1 \times 10^{-5}$ is the optimal parameter where $ICC = 0.604$. Phantom 3 tested the performance of imaging three conductive objects. The three objects tend to cluster in one group if the regularization coefficient exceeds 1×10^{-5} . Although the three ground-truth objects can be visualized by tuning $\alpha = 1 \times 10^{-5}$, they are contaminated with some image artifacts in the reconstructed images. Phantom 4 illustrated a annular flow model. It is most distinguishable at $\alpha = 1 \times 10^{-5}$, and the corresponding $ICC = 0.687$.

VII. CONCLUSION

This paper introduces a magnetic induction imaging system with gradiometer coils as front-end sensors. Through theoretical analysis and numerical simulation, it is proved that the sensitivity of gradiometer coil can be significantly improved by subtracting the primary magnetic field with the differential sensing coils. The experiment results confirmed the capability of the proposed MIT hardware system and the Laplacian regularization for inverse problem. The MIT system is expected to generate high-quality images with proper α for phantom tests. For multi-object and other complicated objects, it is suggested by the results that the spatial solution is lower with obvious reconstructed errors.

The presented MIT system renders possible the non-contact imaging of the electrical conductivity by applying highly resolving hardware and elaborate signal processing. This not only led to further research to image various biomedical applications but also to certain low conductivity industrial process applications like multiphase flow measurement. Future research will focus on accelerating the speed of data acquisition and improving the quality of reconstructed images.

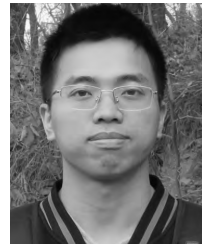
ACKNOWLEDGMENT

The authors would like to thank Prof. Lihui Peng from Tsinghua University for helpful discussions about the whole system design and to thank Mr. Xiaohui Xue and Mr. Hao Xiong for experiment assistance. The authors would also like to express their gratitude towards Dr. Lu Ma for valuable comments that have led to a significant improvement of the manuscript.

REFERENCES

- [1] S. Watson, R. Williams, W. Gough, and H. Griffiths, "A magnetic induction tomography system for samples with conductivities below 10 S m^{-1} ," *Meas. Sci. Technol.*, vol. 19, no. 4, Feb. 2008, Art. no. 045501.
- [2] L. Ma, A. Hunt, and M. Soleimani, "Experimental evaluation of conductive flow imaging using magnetic induction tomography," *Int. J. Multiphase Flow*, vol. 72, pp. 198–209, Jun. 2015.
- [3] S. Wang, R. Hou, J. R. S. Avila, Y. Tao, and W. Yin, "A novel approach to measuring separation process of oil—Saline using differential electromagnetic inductive sensor and FPGA-based impedance analyzer," *IEEE Sensors J.*, vol. 18, no. 19, pp. 7980–7989, Oct. 2018.
- [4] L. Wang and A. M. Al-Jumaily, "Imaging of lung structure using holographic electromagnetic induction," *IEEE Access*, vol. 5, pp. 20313–20318, 2017.
- [5] S. Zhao et al., "An experimental study of relationship between magnetic induction phase shift and brain parenchyma volume with brain edema in traumatic brain injury," *IEEE Access*, vol. 7, pp. 20974–20983, 2019.
- [6] L. Ma, D. McCann, and A. Hunt, "Combining magnetic induction tomography and electromagnetic velocity tomography for water continuous multiphase flows," *IEEE Sensors J.*, vol. 17, no. 24, pp. 8271–8281, Dec. 2017.
- [7] M. Zolgharni, H. Griffiths, and P. D. Ledger, "Frequency-difference MIT imaging of cerebral haemorrhage with a hemispherical coil array: Numerical modelling," *Physiol. Meas.*, vol. 31, no. 8, p. S111, Jul. 2010.
- [8] B. Dekdouk, "Image reconstruction of low conductivity material distribution using magnetic induction tomography," Ph.D. dissertation, School Elect. Electron. Eng., Univ. Manchester, Manchester, U.K., 2011.
- [9] J. Behin and M. Aghajari, "Influence of water level on oil—Water separation by residence time distribution curves investigations," *Separat. Purification Technol.*, vol. 64, no. 1, pp. 48–55, Nov. 2008.
- [10] J. Wang, M. Jia, Z. Lv, Y. Liang, and Z. Li, "Analysis of the magnetic field in the cavity of multi-layer winding electromagnetic water processor," *IEEE Access*, vol. 7, pp. 2512–2519, 2019.
- [11] K. Wei, C.-H. Qiu, and K. Primrose, "Super-sensing technology: Industrial applications and future challenges of electrical tomography," *Philos. Trans. Roy. Soc. A, Math., Phys. Eng. Sci.*, vol. 374, nos. 20–70, Jun. 2016, Art. no. 20150328.
- [12] C. Tan, Y. Wu, Z. Xiao, and F. Dong, "Optimization of dual frequency-difference MIT sensor array based on sensitivity and resolution analysis," *IEEE Access*, vol. 6, pp. 34911–34920, 2018.
- [13] H. Mahdavi and J. Rosell-Ferrer, "In-bed vital signs monitoring system based on unobtrusive magnetic induction method with a concentric planar gradiometer," *Physiol. Meas.*, vol. 38, no. 6, p. 1226, May 2017.
- [14] H. Scharfetter, R. Casanas, and J. Rosell, "Biological tissue characterization by magnetic induction spectroscopy (MIS): Requirements and limitations," *IEEE Trans. Biomed. Eng.*, vol. 50, no. 7, pp. 870–880, Jul. 2003.
- [15] Z. Cui, Y. Chen, P. Zou, C. Wang, and H. Wang, "Development of electromagnetic tomography system using LCR meter," in *Proc. IEEE Int. Instrum. Meas. Technol. Conf. (I2MTC)*, May 2018, pp. 1–5.
- [16] Z. Xu, H. Luo, W. He, C. He, X. Song, and Z. Zahng, "A multi-channel magnetic induction tomography measurement system for human brain model imaging," *Physiol. Meas.*, vol. 30, no. 6, p. S175, Jun. 2009.
- [17] W. Yin, G. Chen, L. Chen, and B. Wang, "The design of a digital magnetic induction tomography (MIT) system for metallic object imaging based on half cycle demodulation," *IEEE Sensor J.*, vol. 11, no. 10, pp. 2233–2240, Oct. 2011.
- [18] H.-Y. Wei and M. Soleimani, "Hardware and software design for a national instrument-based magnetic induction tomography system for prospective biomedical applications," *Physiol. Meas.*, vol. 33, no. 5, p. 863, Apr. 2012.
- [19] Z. Cui, H. Wang, and W. Yin, "Electrical capacitance tomography with differential sensor," *IEEE Sensors J.*, vol. 15, no. 9, pp. 5087–5094, Sep. 2015.
- [20] E. J. Mohamad, "An introduction of two differential excitation potentials technique in electrical capacitance tomography," *Sens. Actuators A, Phys.*, vol. 180, pp. 1–10, Jun. 2012.
- [21] H. Payson et al., "Improved sensitivity and limit-of-detection using a receive-only coil in magnetic particle imaging," *Phys. Med. Biol.*, vol. 63, no. 13, Jul. 2018, Art. no. 13NT02.
- [22] J. Rosell-Ferrer, R. Merwa, P. Brunner, and H. Scharfetter, "A multifrequency magnetic induction tomography system using planar gradiometers: Data collection and calibration," *Physiol. Meas.*, vol. 27, no. 5, p. S271, Apr. 2006.
- [23] M. D. O'Toole, N. Karimian, and A. J. Peyton, "Classification of non-ferrous metals using magnetic induction spectroscopy," *IEEE Trans. Ind. Informat.*, vol. 14, no. 8, pp. 3477–3485, Aug. 2018.
- [24] M. D. O'Toole, L. A. Marsh, J. L. Davidson, Y. M. Tan, D. W. Armitage, and A. J. Peyton, "Non-contact multi-frequency magnetic induction spectroscopy system for industrial-scale bio-impedance measurement," *Meas. Sci. Technol.*, vol. 26, no. 3, Feb. 2015, Art. no. 035102.
- [25] J. Xiang, H. Xiong, and Y. Dong, "Magnetic induction sensing with a gradiometer coil and measurement circuit," in *Proc. IEEE SENSORS*, Oct. 2018, pp. 1–3.

- [26] H.-Y. Wei and A. J. Wilkinson, "Design of a sensor coil and measurement electronics for magnetic induction tomography," *IEEE Trans. Instrum. Meas.*, vol. 60, no. 12, pp. 3853–3859, Dec. 2011.
- [27] H. Wee, S. Watson, R. Patz, H. Griffiths, and R. Williams, "A magnetic induction tomography system with sub-millidegree phase noise and high long-term phase stability," in *Proc. 4th Eur. Conf. Int. Fed. Med. Biol. Eng.*, Oct. 2009, pp. 744–747.
- [28] J. Rosell, R. Casafas, and H. Scharfetter, "Sensitivity maps and system requirements for magnetic induction tomography using a planar gradiometer," *Physiol. Meas.*, vol. 22, no. 1, p. 121, Feb. 2001.
- [29] D. N. Dyck, D. A. Lowther, and E. M. Freeman, "A method of computing the sensitivity of electromagnetic quantities to changes in materials and sources," *IEEE Trans. Magn.*, vol. 30, no. 5, pp. 3415–3418, Sep. 1994.
- [30] S. Tumanski, "Induction coil sensors—A review," *Meas. Sci. Technol.*, vol. 18, no. 3, p. R31, Jan. 2007.
- [31] Z. Xiao, C. Tan, and F. Dong, "Sensitivity comparison of a cambered magnetic induction tomography for local hemorrhage detection," in *Proc. IEEE Int. Symp. Med. Meas. Appl. (MeMeA)*, Jun. 2018, pp. 1–5.
- [32] J. L. Mueller and S. Siltanen, *Linear and Nonlinear Inverse Problems with Practical Applications*. Philadelphia, PA, USA: SIAM, 2012, vol. 10.
- [33] Y. Yang, J. Jia, S. Smith, N. Jamil, W. Gamal, and P.-O. Bagnaninchi, "A miniature electrical impedance tomography sensor and 3-D image reconstruction for cell imaging," *IEEE Sensors J.*, vol. 17, no. 2, pp. 514–523, Feb. 2017.
- [34] D. I. Shuman, S. K. Narang, P. Frossard, A. Ortega, and P. Vandergheynst, "The emerging field of signal processing on graphs: Extending high-dimensional data analysis to networks and other irregular domains," *IEEE Signal Process. Mag.*, vol. 30, no. 3, pp. 83–98, May 2013.



JINXI XIANG received the B.S. degree in measuring and control technology and instrumentation from Wuhan University, in 2016. He is currently pursuing the Ph.D. degree in measurement science and technology with Tsinghua University. His research interests include wearable devices, electrical field sensors, and magnetic induction sensors.



YONGGUI DONG received the B.S. degree in mechanical engineering and the Ph.D. degree in mechatronics from Tsinghua University, Beijing, China, in 1988 and 1994, respectively, where he is currently a Professor and a Ph.D. Supervisor with the Department of Precision Instruments. His current research interests include sensor technology, measurement and test technology, and intelligent instruments technology.



MAOMAO ZHANG received the dual B.Eng. degrees in electrical power engineering from the University of Bath, Bath, U.K., and North China Electrical Power University, Beijing, China, in 2011, the M.Sc. degree in electrical power from the University of Bath, in 2012, and the Ph.D. degree in electrical capacitance tomography and hybrid modality of integrating electrical tomography. His research interests include contactless electromagnetic tomography and multiphase flow measurement.



YI LI received the B.Eng. degree (Hons.) in digital communication from the University of Central Lancashire, Preston, U.K., in 2004, and the Ph.D. degree in electronics and electrical engineering from The University of Manchester, Manchester, U.K., in 2008. Since 2014, he holds a lectureship position with Tsinghua University, Beijing, China. He is currently establishing a key laboratory for subsea gas–oil–water multiphase flow measurement for oceanic oil and gas exploration and production. His research interests include electrical capacitance and resistance tomography, gas–oil–water multiphase flow measurement, and gas–solids multiphase flow measurement.

• • •